



# Ultrafast spallation dynamics of a thin gold film characterized by imaging pump-probe interferometry

Theo Pflug<sup>1</sup> · Markus Olbrich<sup>1</sup> · Henry Loheit<sup>1</sup> · and Alexander Horn<sup>1</sup>

Received: 22 April 2024 / Accepted: 3 August 2024  
© The Author(s) 2024

## Abstract

Interferometry allows to measure microscopic displacements in the nanometer scale. This work introduces an imaging pump-probe interferometer that enables to detect the spatially resolved phase shift of the probe radiation being reflected on a sample surface after ultrashort pulsed laser excitation with a temporal resolution of 40 fs and a maximum temporal delay of 3 ns. The capability of the pump-probe interferometer is demonstrated on the spallation of a thin gold film upon femtosecond laser irradiation. The pump-probe interferometer enables to measure a minimum phase change of  $\Delta\varphi < \pi/10$  which corresponds to a displacement of  $\Delta h < 12.5$  nm for the applied probe wavelength of 500 nm. Upon irradiation, two distinct phase changes are observable: First, an abrupt minor phase shift has been measured in the femtosecond range, which is attributed to the changed optical properties of the sample surface after excitation. Second, a more pronounced continuing phase shift increase is detectable after a few tens of picoseconds resulting from the onset of spallation. Based on the measured spatially resolved phase shift, the transient surface topography during the spallation is reconstructed. The determined velocity of the ablated material reaches a maximum of a few 1000 m/s at ten picosecond after irradiation and decreases to 250 m/s afterwards. Consequently, the introduced imaging pump-probe interferometer provides important insights into the physical processes during laser excitation as well as the subsequent laser-induced ablation, and will enable to validate theoretical models quantitatively in following studies.

**Keywords** Pump-probe interferometry · Spatially resolved · Femtosecond laser radiation · Ablation velocity · Spallation

## 1 Introduction

The time-resolved pump-probe technique represents an established tool to investigate ultrafast dynamical processes during and after the interaction of matter with femtosecond laser radiation [1–9]. Pump-probe microscopy employs probe radiation to measure the optical response of a sample material due to the irradiation with pump laser radiation. Laser radiation predominantly interacts with the electrons of the material due to their three orders of magnitude smaller mass in comparison to the atomic nuclei. As the exciting radiation is partially absorbed, the electron system is heated, leading to an abruptly increasing electron temperature, whereas the lattice remains approximately at room temperature [10–12]. The electron system only gradually transfers

energy to the lattice by electron–phonon collisions. After a few picoseconds in the range of the electron–phonon relaxation time, the electron system and the lattice exhibit similar temperatures [10, 12–14].

Subsequently, the material is ablated, if the amount of absorbed energy of the pump laser radiation is larger than a material specific threshold. Thereby, the two well-known processes spallation and phase explosion represent the driving mechanism for ablation [8, 12, 15–22]. Spallation refers to the ablation of a closed layer of liquid material with foam-like material underneath. For the case that the exciting pump radiation features a Gaussian-shaped spatial fluence distribution, spallation leads to bulging of the ablated layer until it tears off from the surrounding material [12, 23]. Phase explosion occurs at even larger peak fluences of the pump radiation, when the lattice temperature exceeds approximately 90 % of a thermodynamic critical temperature [19, 24–26]. Then, the ablated material is transformed into a liquid–vapor mixture and expands explosively in all directions, whereby the most

✉ Theo Pflug  
pflug@hs-mittweida.de

<sup>1</sup> Laserinstitut Hochschule Mittweida, Hochschule Mittweida, Technikumplatz 17, 09648 Mittweida, Germany

pronounced expansion direction is represented towards the ambient material. [16–20, 22, 23].

To investigate the described physical processes, the pump-probe principle has been combined with various optical metrology methods. In the early time scales of a few femtoseconds to picoseconds after the excitation, the initial topography of the sample is still preserved and thus pump-probe ellipsometry allows to measure the transient optical properties of the excited material surface [1, 2, 4, 6, 27]. At later times, pump-probe reflectometry enables to characterize the transient ablation topography by analyzing the observed Newton rings [3, 8, 15, 23, 28]. These Newton rings represent characteristic interference patterns that result from the interference of the probe radiation being partially reflected on the top of the ablated material layer and on the top of the remaining material underneath [8, 23]. Therefore, observing and analyzing Newton rings requires the thickness of the ablated material layer to be in the range of a few multiples of the optical penetration depth of the probe radiation. Vice versa, when the thickness of the ablated material layer is much larger than the optical penetration depth, no Newton rings can be observed and thus the transient topography of the material surface during ablation cannot be reconstructed unambiguously by applying pump-probe reflectometry solely.

To circumvent this limitation, this study introduces an imaging pump-probe interferometer that allows to measure the phase shift of probe radiation being reflected on the excited sample surface. The interferometer setup is based on the principles demonstrated in previous studies [5, 29–33]. The capability of the interferometer is demonstrated on a thin gold film that has been irradiated by femtosecond pump laser radiation. The thickness of the ablated material layer is approximately four times the optical penetration depth of the applied probe radiation, and thus no Newton rings are observable. Therefore, the transient phase shift during excitation and ablation is reconstructed by analyzing the measured interference patterns. Two new methods for analyzing the measured interference patterns are introduced in this study. Evaluation method 1 derives the laser-induced phase shift by comparing the interference patterns with and without excitation, enabling a resolution of  $\Delta\varphi < \pi/10$ . Evaluation method 2 mathematically reconstructs the measured interference patterns allowing to determine the spatial phase shift distribution for large maximum phase shifts of  $\Delta\varphi > 2\pi$ . The characterization of the measured time-resolved interference patterns upon pump laser irradiation enables to clearly distinguish between the phase shift being induced by the excitation of the electrons system (optical), and the phase shift resulting from bulging of the sample surface due to the onset of ablation (topographical).

In the following, the interferometric setup and the applied methods for evaluating the measured data are explained in

detail. Afterwards, the experimental results considering the ablation dynamics of a thin gold film are demonstrated and discussed.

## 2 Materials and methods

### 2.1 Experimental setup

The pump-probe setup (Fig. 1a) employs an amplified Ti:sapphire laser system (Coherent Inc., Astrella) providing ultrashort pulsed laser radiation with the pulse duration  $\tau_H = 35$  fs, the wavelength  $\lambda = 800$  nm, the pulse energy  $Q_p = 7.5$  mJ, and the beam propagation rate  $M^2 \geq 1.2$ . The

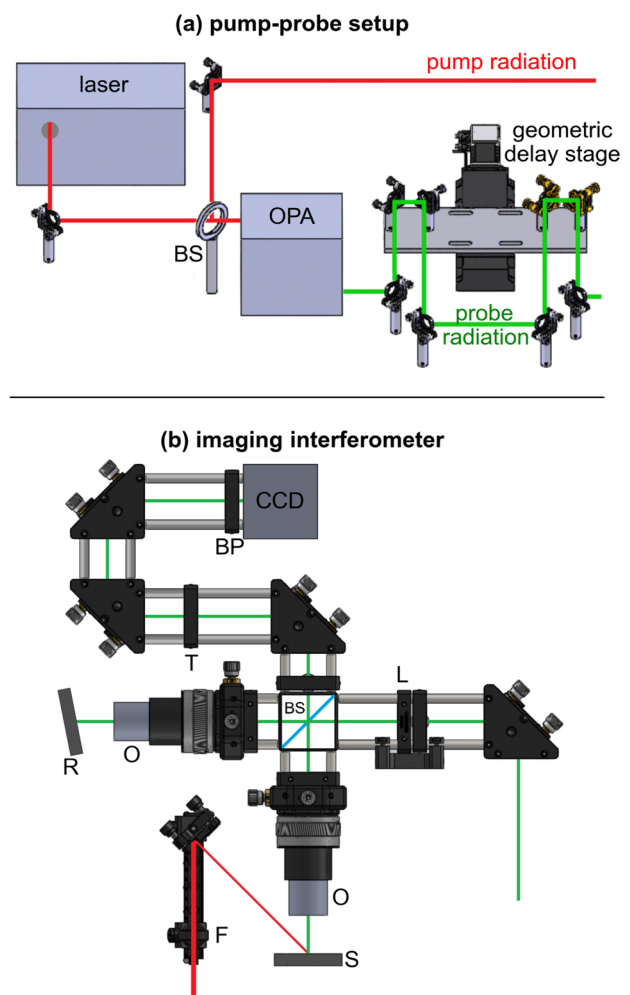


**Fig. 1** **a** Schematic setup for generating pump (red) and probe radiation (green) consisting of the laser, the beamsplitter BS, the optical parametric amplifier OPA, and a geometrical delay stage. **b** Scheme of the imaging pump-probe interferometer with the lens L, the microscope objectives O, the sample surface S, the reference surface R, the focusing lens F, the tube lens T, the bandpass filter BP, and the CCD camera

radiation is divided into pump and probe radiation by a beam splitter (Fig. 1a BS). An optical parametric amplifier (OPA, Light Conversion Inc., TOPAS Prime) enables to change the wavelength of the probe radiation between 250 nm and 20  $\mu\text{m}$ . In this study, the wavelength of the probe radiation is set to  $\lambda_{\text{probe}} = 500$  nm, the wavelength of the pump radiation remains unchanged at  $\lambda_{\text{pump}} = 800$  nm. The pulse energy of both pump and probe radiation can be varied by external attenuators (Altechna Co. Ltd., Watt Pilot). An geometric delay stage allows to change the optical path length of pump and probe radiation relatively to each other resulting in a maximum temporal delay of 3 ns with a temporal step width of 40 fs. The spatial, spectral, and temporal properties of the pump and probe radiation have been characterized in more detail in previous studies [27, 34].

The pump radiation is focused onto the sample surface under an angle of incidence of approximately  $\theta = 50^\circ$  by using a focusing lens (Fig. 1b F, focal length 150 mm), as measured and demonstrated in a previous study [9, 23]. The investigated sample consists of a 150 nm gold film deposited on a fused silica substrate with a 20 nm chromium adhesion layer in between. In this study, the thin gold film is irradiated with a peak fluence of the pump radiation of  $H_0 = 1.35 \text{ J/cm}^2 = 1.5 H_{\text{thr}}$ . The ablation threshold fluence  $H_{\text{thr}}$  of the sample has been determined by the method of the squared diameter (Fig. 2a [35]) resulting to  $H_{\text{thr}} = (0.9 \pm 0.1) \text{ J/cm}^2$ . The determined circle equivalent beam radius has been determined to  $w_0 = (27.0 \pm 0.2) \mu\text{m}$ . Due to the angle of incidence  $\theta$ , an elliptical ablation structure is generated with an ellipticity of 0.81 (Fig. 2b). Considering the ellipticity and the circle equivalent beam radius  $w_0$ , the beam dimensions along

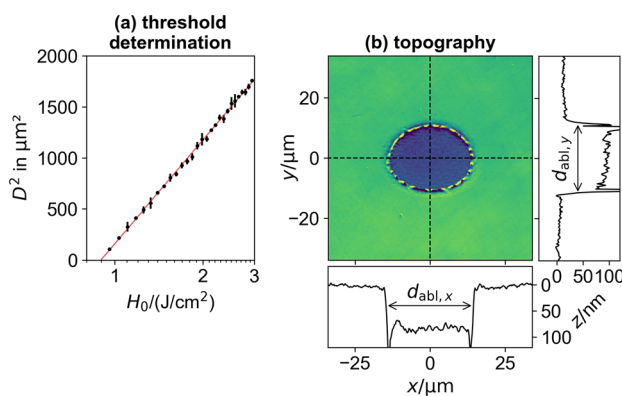


**Fig. 2** **a** Squared circle-equivalent diameter  $D^2$  of the ablation structures in gold generated by single-pulse irradiation depending on the peak fluence  $H_0$  of the pump radiation [35]. The resulting circle equivalent beam radius is  $w_0 = (27.0 \pm 0.2) \mu\text{m}$ , the determined ablation threshold fluence of gold is  $H_{\text{thr}} = (0.9 \pm 0.1) \text{ J/cm}^2$ . **b** Ablation structure in gold after pump irradiation at the peak fluence  $H_0 = 1.35 \text{ J/cm}^2 = 1.5 H_{\text{thr}}$

the major and minor axes result to  $w_{0,x} = 30.1 \mu\text{m}$  and  $w_{0,y} = 24.3 \mu\text{m}$ .

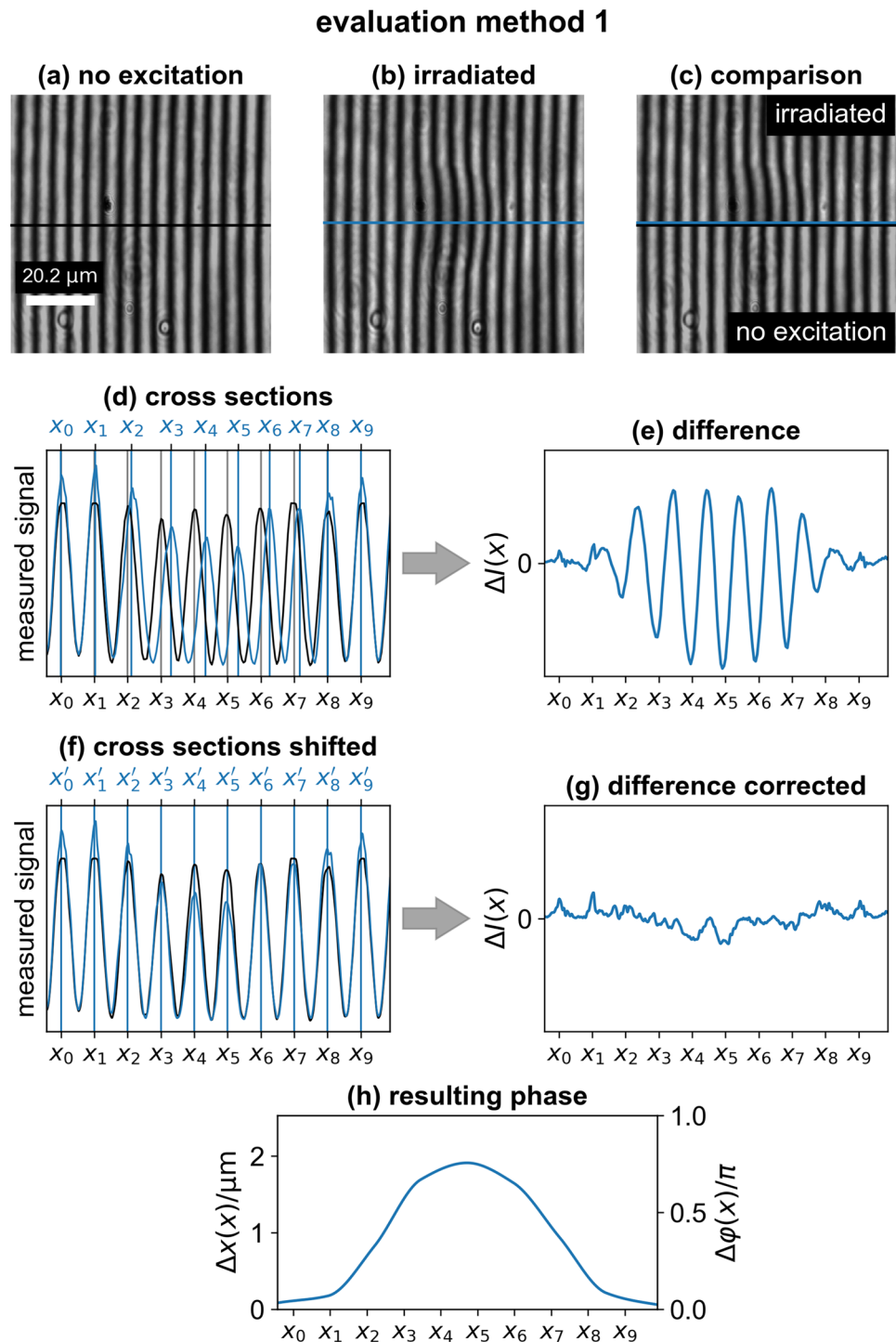
The single-pulse irradiation of the gold film results in a flat ablation structure with an almost constant depth of  $d_{\text{abl},z} = (79 \pm 5) \text{ nm}$  and the lateral dimensions  $d_{\text{abl},x} = 29.4 \mu\text{m}$  and  $d_{\text{abl},y} = 23.8 \mu\text{m}$  (Fig. 2b). In order to characterize the dynamical processes during the ablation, imaging pump-probe interferometry is employed. Therefore, the probe radiation is guided into the imaging interferometer (Fig. 1b) in which a beam splitter BS divides the probe radiation into two parts. The reflected part propagates through a microscope objective O (Nikon, TU Plan ELWD, 20 $\times$ , NA = 0.4) and is reflected on the sample surface S. In the following, this part of the probe radiation is referred to as sample beam. The transmitted part propagates through an identical objective and is reflected on a reference surface R being identical to the sample S. This part of the probe radiation is referred to as reference beam. The illuminated surfaces of both sample S and reference R are then imaged onto the CCD camera (1280  $\times$  1024 pixel, pixel size 4.8  $\mu\text{m} \times 4.8 \mu\text{m}$ ) via the objectives O and a tube lens T with a focal length of 200 mm. A bandpass filter BP (center wavelength 500 nm, FWHM bandwidth 40 nm) prevents the detection of any scattered pump radiation. The lens L with a focal length of 150 mm is located 190 mm before both microscope objectives and allows to adjust the beam size of the probe radiation on the sample and reference surface and thus, enables a homogeneous illumination of the CCD camera.

As the optical beam path lengths between the sample and reference surface and the CCD camera are identical for both the sample and reference beam, the detected image results from the interference of these two beams. The reference surface R is slightly tilted to generate a characteristic interference pattern with fringes parallel to the y-axis. These parallel fringes will be shifted, when the optical or topographical properties of the sample surface S, and thus the phase between the sample and reference beam, change due to the excitation by pump laser radiation. Therefore, the time-resolved evaluation of the measured transient interference pattern gives insights into the dynamical processes during laser excitation and the subsequent ablation. The evaluation of the interference patterns is explained more detailed in the following section.

## 2.2 Data evaluation

Without excitation due to pump irradiation, the optical and topographical properties of the sample surface S are identical to those of the reference surface R. Since the reference surface R is tilted by 2.8° relative to the incident probe radiation, the interfering sample and reference beams result in straight interference fringes with a spatial periodicity of  $\lambda_x = 5.05 \mu\text{m}$  (Fig. 3a). When exciting the sample surface

**Fig. 3** **a** Measured interference pattern without pump excitation of the sample surface. **b** Measured interference pattern 306 ps after irradiation of the sample surface. **c** Comparison of the interference patterns with and without irradiation. **d** Cross-sections of the interference patterns from **c**. The blue lines correspond to the interference pattern after irradiation, the black lines to the patterns without excitation. **e** Difference  $\Delta I(x)$  of the measured interference patterns. **f** Comparison of the interference pattern without excitation with interference pattern with irradiation with the shifted  $x$ -coordinates. **g** Difference  $\Delta I(x)$  of the measured interference pattern without excitation with the shifted interference patterns with irradiation. **h** The shift function  $\Delta x(x)$  and the corresponding phase shift  $\Delta\varphi(x)$



S with incident pump radiation, the sample topography as well as its optical properties change, resulting in a phase shift of the reflected sample beam. This spatially dependent phase shift  $\Delta\varphi(x, y)$  leads to a curvature of the initially straight interference fringes (Fig. 3b). This laser-induced phase shift  $\Delta\varphi(x, y)$  can be reconstructed by comparing the measured interference patterns with and without irradiation (Fig. 3c). For schematically demonstrating the procedure for

reconstructing  $\Delta\varphi(x, y)$ , the cross-sections of both interference patterns are shown in Fig. 3d in which the positions of the maxima are assigned to the variables  $x_i$ . The maxima of the reference measurement without irradiation are indicated by black variables, the maxima of the measurement with irradiation in blue. The difference between the measured interference patterns with and without irradiation  $\Delta I(x)$  is demonstrated in Fig. 3e. In order to derive the phase shift

$\Delta\varphi$ , the positions of the maxima  $x_i$  (Fig. 3f blue) are shifted by a shift function  $\Delta x(x)$  in order to superimpose the maxima and minima of the interference patterns with and without irradiation (Fig. 3f), resulting in the shifted positions  $x'_i$  and a reduction of the calculated difference  $\Delta I(x)$  (Fig. 3g). The shift function  $\Delta x(x)$  is represented by a polynomial function that is refined to minimize  $\Delta I(x)$  (Fig. 3h). Finally, the phase shift  $\Delta\varphi(x)$  is calculated by

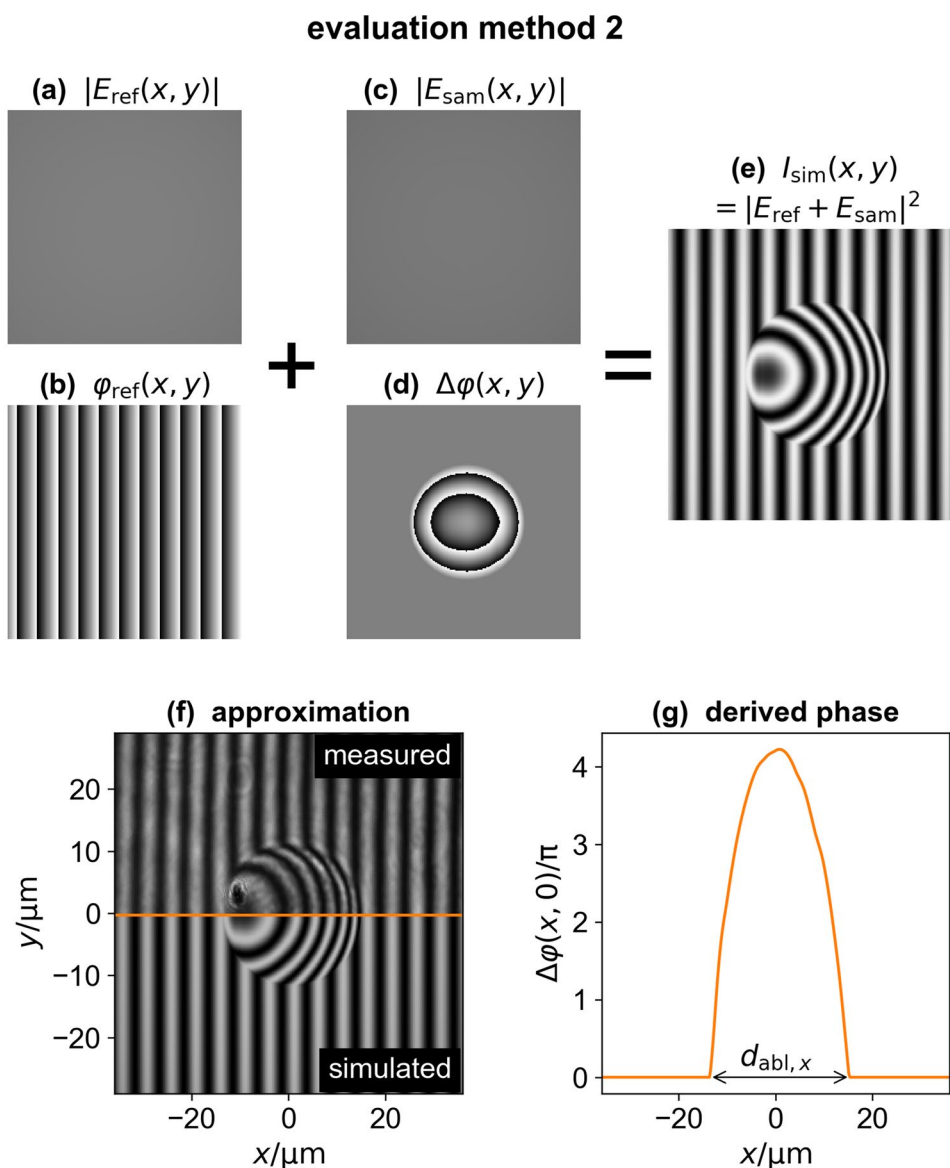
$$\Delta\varphi(x) = \frac{2\pi \Delta x(x)}{\lambda_x} \tag{1}$$

considering the shift function  $\Delta x(x)$  and the spatial periodicity  $\lambda_x$  of the interference pattern without irradiation.

The previously described method is only feasible, when the maximum phase shift is  $\Delta\varphi_{\max} < 2\pi$ . Otherwise

additional interference fringes would appear causing the reconstruction to be ambiguous. Therefore, a second evaluation method is applied to reconstruct the spatially resolved phase shift  $\Delta\varphi(x, y)$  of the sample beam after pump laser excitation by approximating a simulated interference pattern to the measured one. In principle, the electrical field strength reflected on the reference surface R can be described by  $E_{\text{ref}} = |E_{\text{ref}}(x, y)| \cdot \exp(i\varphi_{\text{ref}}(x, y))$ , as demonstrated in Fig. 4a, b. Analogous, the electrical field strength of the sample beam is described by  $E_{\text{sam}} = |E_{\text{sam}}(x, y)| \cdot \exp(i\Delta\varphi(x, y))$  (Fig. 4c, d). In the experimental setup, the phase shift  $\varphi_{\text{ref}}(x, y)$  results from the tilted reference surface R (Fig. 1b), whereas  $\Delta\varphi(x, y)$  is induced by a change in the optical and topographical properties of the sample surface S due to the pump irradiation. The superposition of both electrical field strengths results then in the simulated intensity distribution

**Fig. 4** **a, b** Spatial electrical field distribution  $|E_{\text{ref}}(x, y)|$  and the corresponding phase  $\varphi_{\text{ref}}(x, y)$  of the reference beam. **c, d** Spatial electrical field distribution  $|E_{\text{sam}}(x, y)|$  and the corresponding phase  $\varphi_{\text{sam}}(x, y)$  of the sample beam. **e** Resulting spatial intensity distribution  $I_{\text{sim}}(x, y)$ . **f** Comparison of the measured and simulated intensity distributions. **g** Cross-section of the reconstructed spatially resolved phase shift  $\Delta\varphi(x, y = 0)$



$I_{\text{sim}}(x, y) = |E_{\text{ref}} + E_{\text{sam}}|^2$  (Fig. 4e). The simulated spatial intensity distribution  $I_{\text{sim}}(x, y)$  is then approximated to the measured interference pattern (Fig. 4f) with the phase of the sample beam  $\Delta\varphi(x, y)$  representing a refinable polynomial. The cross-section of an exemplary reconstructed phase shift  $\Delta\varphi(x, y = 0)$  is demonstrated in Fig. 4g. For simplicity,  $\Delta\varphi(x)$  is only refined within the area in which the thin gold film is ablated corresponding to  $|x| \leq d_{\text{abl},x}/2$ .

This simple model is able to reconstruct the measured interference patterns quite well, because the thickness of the ablated film  $d_{\text{abl},z} = (79 \pm 5)$  nm is approximately 4 times the optical penetration depth  $d_z(\lambda_{\text{probe}} = 500 \text{ nm}) = 21 \text{ nm}$  by assuming a constant complex refractive index of  $\tilde{n} \approx 1 - 2i$  [2]. Therefore, the characterization of thinner films being ablated or more complex ablation processes, such as phase explosion, would require the application of the transfer matrix formalism [23, 34].

One should note, the Fourier-transform method published in the literature [36] represents another technique for analyzing the measured interference patterns and deriving the laser-induced phase shift. However, for the experimental data presented in this study, the Fourier-transform method resulted in ambiguous solutions of the phase distributions when the maximum phase shift was  $\Delta\varphi_{\text{max}} < \pi/5$ . Therefore, the Fourier-transform method has not been applied in this study.

### 2.3 Validation of the interferometer

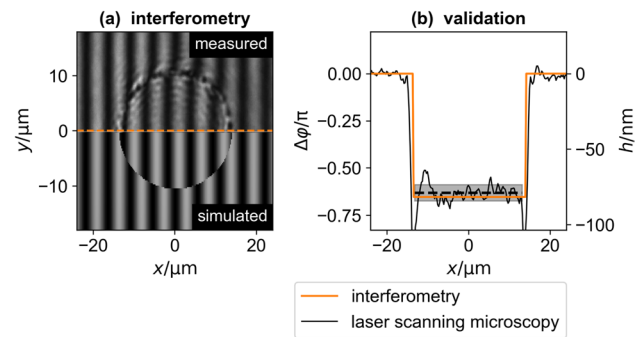
To validate the interferometric measurement, the topography of the final ablation structure in gold after pump laser irradiation is reconstructed by interferometry and measured by laser scanning microscopy for comparison. The interference pattern resulting from the ablation structure is reconstructed by the evaluation method 2 from Sect. 2.2 as demonstrated in Fig. 5a. Based on the derived phase shift  $\Delta\varphi(x, y)$  the transient topography of the ablation structure is derived by

$$\Delta h(x, y) = \Delta\varphi(x, y) \frac{\lambda_{\text{probe}}}{4\pi} \quad (2)$$

considering the wavelength of the probe radiation  $\lambda_{\text{probe}} = 500 \text{ nm}$ . The resulting ablation depth determined by interferometry is approximately 80 nm (Fig. 5b orange line) being close to the ablation depth  $d_{\text{abl},z} = (79 \pm 5)$  nm measured by laser scanning microscopy (Fig. 5b black line).

## 3 Results and discussion

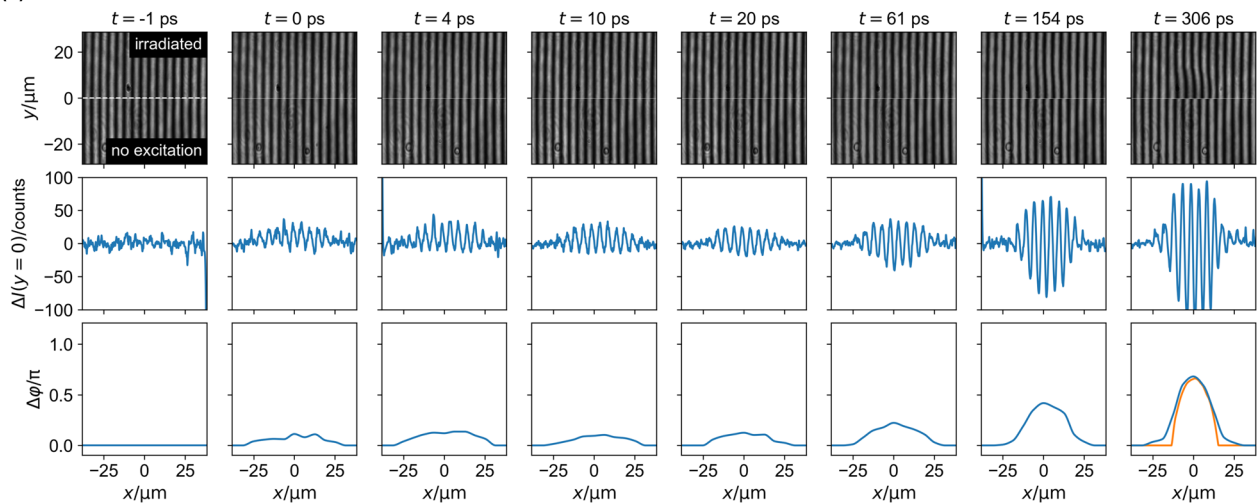
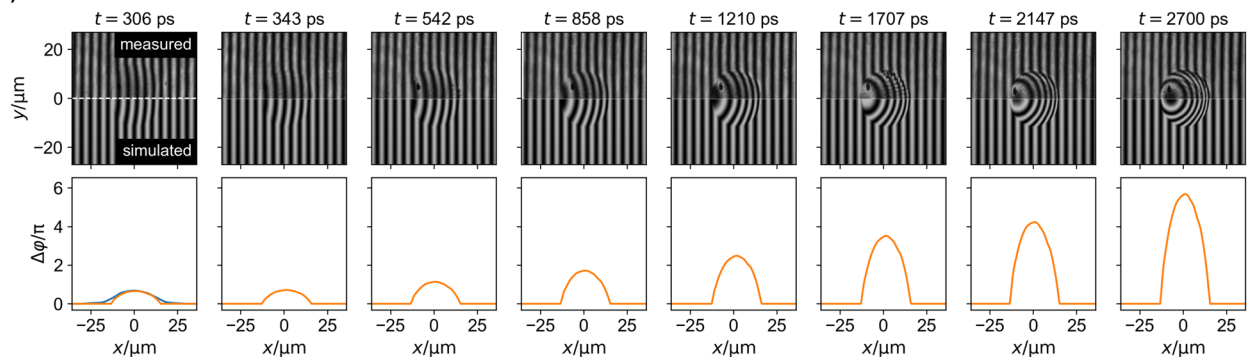
A thin gold film (150 nm gold on 20 nm chromium deposited on a fused silica substrate) has been irradiated by pump laser radiation ( $\lambda_{\text{pump}} = 800 \text{ nm}$ ,  $\tau_{\text{H}} = 40 \text{ fs}$ ,  $H_0 = 1.35 \text{ J/cm}^2 = 1.5H_{\text{thr}}$ ). The temporal dynamics during the



**Fig. 5** **a** Measured and simulated interference pattern of the final ablation structure in gold after pump laser irradiation. **b** Comparison of the height profile  $h(x, y = 0)$  being reconstructed from the interferometric measurement and measured by laser scanning microscopy. The black dotted line represents the mean value of the ablation depth, the gray area corresponds to its standard deviation

excitation and ablation processes has been investigated by imaging pump-probe interferometry within the time range  $-1 \text{ ps} \leq t \leq 3 \text{ ns}$ . The probe radiation features the wavelength  $\lambda_{\text{probe}} = 500 \text{ nm}$  and the pulse duration  $\tau_{\text{H}} = 40 \text{ fs}$ . Examples of the measured interference patterns are given in Fig. 6a, b. Here, the time at which the maximum intensities of pump and probe radiation interact with the sample surface is assigned to  $t = 0$ . The derivation procedure of  $t = 0$  has been described more detailed in previous studies [11, 27]. The interference patterns measured between  $-1 \text{ ps}$  and  $306 \text{ ps}$  after pump laser irradiation have been analyzed by evaluation method 1 from Sect. 2.2 (Fig. 6a). For later times between  $306 \text{ ps}$  and  $2700 \text{ ps}$ , method 2 has been adopted for evaluation (Fig. 6b).

Before pump irradiation, at  $-1 \text{ ps}$ , no significant difference  $\Delta I$  between the interference patterns measured with and without irradiation is detectable, and therefore the reconstructed phase shift is  $\Delta\varphi \approx 0$ . In contrast, between  $0 \text{ ps}$  and  $20 \text{ ps}$  after irradiation, the difference  $\Delta I$  increases within the irradiated area, and thus also the resulting phase shift  $\Delta\varphi$  increases slightly and sustains an almost constant maximum value of  $\Delta\varphi \approx 0.15\pi$ . For  $t \geq 61 \text{ ps}$ , the maximum phase shift increases further and the diameter of the spatial phase shift distribution decreases. The broader spatial phase shift distribution with an almost constant maximum between  $0$  and  $20 \text{ ps}$  most probably results from the excitation of the electron system and the accompanied changed complex refractive index  $\tilde{n}$  [2]. According to the Fresnel equations, a changing  $\tilde{n}$  results in a phase shift of the reflected probe radiation, when the imaginary part of  $\tilde{n}$ , namely the extinction coefficient, is greater than zero. Thus,  $\Delta\varphi$  can increase without any change in the sample surface topography needed. The further increase of the maximum phase shift between  $61 \text{ ps}$  and  $306 \text{ ps}$  cannot result from an additional change of  $\tilde{n}$ , as the laser

**(a) evaluation method 1****(b) evaluation method 2**

**Fig. 6 a** Top row: comparison of the measured interference patterns before and after single-pulsed pump laser irradiation ( $\lambda_{\text{pump}} = 800$  nm,  $\tau_{\text{H}} = 40$  fs,  $H_0 = 1.35$  J/cm $^2 = 1.5H_{\text{thr}}$ ) of a thin gold film at different delay times between pump and probe radiation. The wavelength of the probe radiation is  $\lambda_{\text{probe}} = 500$  nm, the pulse duration  $\tau_{\text{H}} = 40$  fs. Middle row: Difference  $\Delta I$  of the measured interference patterns at  $y = 0$ . Bottom row: resulting spatial phase shift  $\Delta\phi$  at  $y = 0$  reconstructed by evaluation method 1 (blue lines). At the  $t = 306$

ps, the phase shift determined by evaluation method 2 is plotted for comparison (orange line). **b** Top row: comparison of the measured interference patterns and the patterns simulated by evaluation method 2 after single-pulsed pump laser irradiation. The beam properties of pump and probe radiation are equal to **a**. Bottom row: reconstructed phase shift  $\Delta\phi$  at  $y = 0$  (orange lines). At the  $t = 306$  ps, the phase shift determined by evaluation method 1 is plotted for comparison (blue line)

excitation as well as the electron–phonon coupling, both affecting  $\tilde{n}$ , are already completed in this temporal range [37]. Therefore, this further increasing phase shift is attributed to a topographical change due to the onset of ablation.

At  $t = 306$  ps, the spatial phase shift distributions  $\Delta\phi$  derived from both evaluation method 1 and 2 are compared with each other (blue and orange lines at  $t = 306$  ps in Fig. 6a, b). Both evaluation methods provide comparable results, with slight deviations on the flanks of the distributions. This deviation results from the simplification of evaluation method 2, in which only the area with occurring ablation is considered during the approximation of  $\Delta\phi$ , whereas the area surrounding the ablation is also affected by heating and the accompanied change of  $\tilde{n}$  [12]. As the phase shift due to changing  $\tilde{n}$  remains approximately constant (0 to 20 ps in

Fig. 6a), whereas the phase shift resulting from a bulged surface topography due to ablation steadily increases within the considered temporal range (306–2700 ps in Fig. 6b), the error on the flanks of the phase shift distribution becomes negligible. Therefore, evaluation method 2 provides a very good agreement between the simulated and measured interference patterns for later time delays (Fig. 6b).

Previous studies have revealed that during spallation of a thin film, the ablated layer features a closed surface, whereas phase explosion results in the complete decomposition of the ablated layer [23]. Therefore, material being ablated by phase explosion would scatter the probe radiation, resulting in a strong decrease of the reflectance. As the observed interference patterns are well pronounced within the whole considered temporal range and the reflectance of

the sample surface inside the irradiated area is not decreasing strongly, the increasing maximum of the derived phase shift  $\Delta\varphi$  between 61 ps and 2700 ps most certainly results from the ablation of the gold film due to the spallation of a closed layer of gold.

The different origins of the measurable phase shift, resulting either from changed optical properties of the sample surface or ablation, are also visible when considering the maximum phase shift  $\Delta\varphi_{\max}$  as a function of time (Fig. 7). Upon pump laser irradiation, the maximum phase shift increases abruptly to  $\Delta\varphi_{\max} \approx 0.15\pi$  within a few hundred femtoseconds, and sustains an approximately constant value until 10 ps. As mentioned before, the phase shift in this time range (Fig. 7 blue area) predominantly results from a changed complex refractive index due to heating of the electron system. After the electron–phonon coupling, with an electron–phonon relaxation time of  $\tau_R \approx 10$  ps for gold [12, 37], a second increase of  $\Delta\varphi_{\max}$  is detectable, resulting from the topographical change due to the onset of spallation [12] (Fig. 7 white area).

As the increase of  $\Delta\varphi_{\max}$  predominantly results from spallation for times  $t \geq 10$  ps, the maximum height of the ablated sample surface in the center of the irradiated area can be calculated by using Eq. 2 (Fig. 8a). Here, a constant offset  $\Delta\varphi_{\max} = 0.12\pi$  being attributed to the changed optical properties resembles a pseudo height of  $h_{\max, \text{off}} = 15$  nm. This offset  $h_{\max, \text{off}}$  has been subtracted from the values demonstrated in (Fig. 8a). The offset  $h_{\max, \text{off}} = 15$  nm is assumed to be constant as a first order approximation, as a previous study revealed that the optical properties of gold are approximately constant between 20 ps and 2 ns after irradiation at  $H_0 = 1.5 H_{\text{thr}}$  [2].

The corresponding time-dependent velocity of the ablated material was calculated by  $v_{\max} = dh_{\max}/dt$  (Fig. 8b). Shortly after  $t = 10$  ps, the ablation velocity reaches its maximum of

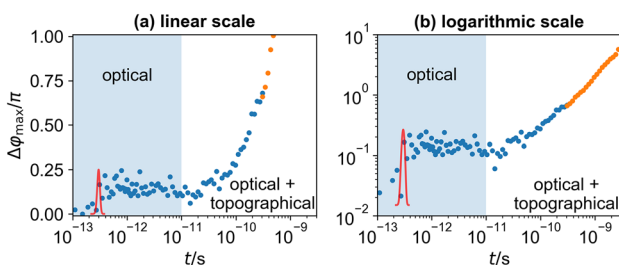


**Fig. 7** Maximum of the reconstructed phase shift  $\Delta\varphi_{\max}$  as a function of time demonstrated with a linear (a) and logarithmic scale (b). The blue dots indicate the values being reconstructed by evaluation method 1 from Sect. 2.2, the orange dots refer to evaluation method 2. The red distribution schematically indicates the temporal intensity distribution of the pump laser radiation. The phase shift within the blue area predominantly results from the change of the optical properties, whereas the white area is affected by both changing optical and topographical properties of the sample surface

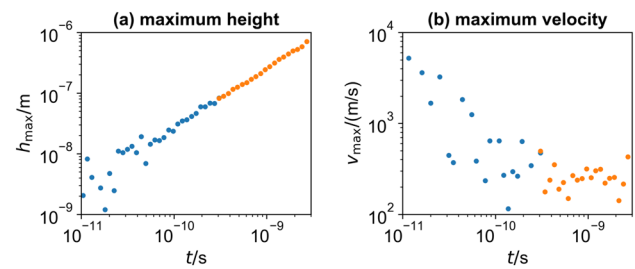


**Fig. 8** a Maximum height of the ablated material in the center of the irradiated area for the times  $t \geq 10$  ps derived by Eq. 2. b Corresponding maximum velocity of the ablated material. The blue dots indicate the values being reconstructed by evaluation method 1 from Sect. 2.2, the orange dots refer to evaluation method 2

a few 1000 m/s and decreases steadily until  $v_{\max} \approx 250$  m/s. The decrease in ablation velocity most probably results from deceleration due to air resistance and the deceleration caused by the surrounding material, which is still connected to the ablated material film [38]. Afterwards, the ablation velocity remains approximately constant within the considered temporal range between 300 ps and 3 ns. This observed slope is very similar to a previous study considering the ablation dynamics of a thin chromium film after femtosecond laser radiation with a comparable fluence of  $H_0 = 1.5 H_{\text{thr}}$  [23].

## 4 Conclusion

In this study, an imaging pump-probe interferometry has been introduced allowing to detect phase changes of  $\Delta\varphi < \pi/10$  spatially resolved. The capability of the interferometer is demonstrated on a thin gold film (150 nm gold on 20 nm chromium deposited on a fused silica substrate), which has been irradiated by single-pulsed pump laser radiation ( $\lambda_{\text{pump}} = 800$  nm,  $\tau_H = 40$  fs,  $H_0 = 1.35$  J/cm<sup>2</sup> =  $1.5 H_{\text{thr}}$ ). The wavelength of the applied probe radiation was  $\lambda_{\text{probe}} = 500$  nm and the temporal delay between pump and probe radiation has been varied between -1 ps to 3 ns with a temporal step width of 40 fs.

Based on the measured interference patterns, the spatially resolved phase shift of the probe radiation being reflected on the sample surface has been reconstructed. Thereby, two distinct time regimes have been identified. First, a minor but abrupt increase of the phase shift was detected directly upon irradiation in the femtosecond range. This phase change most certainly results from the changed complex refractive index of the sample surface due to excitation of the electron system. After a few ten picoseconds being in the range of the electron–phonon relaxation time, the measured phase shift increases once again even further. This second increase is attributed to the onset of spallation and the elevating sample surface. Consequently, the measured phase shift in the



femtosecond to picosecond range purely results from the transient optical properties of the excited sample surface, whereas the phase shift at later time results from both optical and topographical changes. Based on the measured spatially resolved phase shift, the surface topography of the ablated material has been reconstructed. As the interference fringes are well pronounced within the whole considered temporal range and no decrease in the intensity of the measured signal due to scattering has been observed, the material is most certainly ablated by spallation.

In following studies, the presented imaging pump-probe interferometer can also provide deep insights into more complex ablation processes, e.g., a superposition of spallation and phase explosion at higher peak fluences. Then, the evaluation methods have to be expanded by implementing a transfer matrix formalism in order to be able to describe possible occurring density gradients in the ablation plume.

In summary, the presented metrology enables to quantitatively determine the transient ablation topography and the corresponding velocity. Thus, it is applicable to validate theoretical models that describe the excitation and ablation dynamics during and after the interaction of laser radiation with matter.

**Acknowledgements** The authors gratefully thank the German Research Foundation (DFG) for funding the projects no. 469106482 and no. 458053570.

**Author Contributions** Conceptualization: TP, MO, AH; Methodology: TP, HL; Formal analysis and investigation: TP; Writing - original draft preparation: TP; Funding acquisition: AH; Resources: AH; Supervision: AH

**Funding** Open Access funding enabled and organized by Projekt DEAL.

**Data availability** The data presented in this study are available on request from the corresponding author.

## Declarations

**Conflict of interest** The authors declare no conflict of interest.

**Open Access** This article is licensed under a Creative Commons Attribution 4.0 International License, which permits use, sharing, adaptation, distribution and reproduction in any medium or format, as long as you give appropriate credit to the original author(s) and the source, provide a link to the Creative Commons licence, and indicate if changes were made. The images or other third party material in this article are included in the article's Creative Commons licence, unless indicated otherwise in a credit line to the material. If material is not included in the article's Creative Commons licence and your intended use is not permitted by statutory regulation or exceeds the permitted use, you will need to obtain permission directly from the copyright holder. To view a copy of this licence, visit <http://creativecommons.org/licenses/by/4.0/>.

## References

1. S. Rapp, M. Kaiser, M. Schmidt, H.P. Huber, Ultrafast pump-probe ellipsometry setup for the measurement of transient optical properties during laser ablation. *Opt. Express* **24**, 17572–17592 (2016)
2. T. Pflug, J. Wang, M. Olbrich, M. Frank, A. Horn, Case study on the dynamics of ultrafast laser heating and ablation of gold thin films by ultrafast pump-probe reflectometry and ellipsometry. *Appl. Phys. A* **124**, 17572–17579 (2018)
3. Y. Fuentes-Edfuf, M. Garcia-Lechuga, J. Solis, J. Siegel, Ultrafast electron dynamics and optical interference tomography of laser excited steel. *Laser Photon. Rev.* 2200511 (2022)
4. O. Herrfurth et al., Femtosecond-time-resolved imaging of the dielectric function of Zn in the visible to near-ir spectral range. *Appl. Phys. Lett.* **115**, 212103 (2019)
5. V.V. Temnov, K. Sokolowski-Tinten, P. Zhou, D. Linde, Ultrafast imaging interferometry at femtosecond-laser-excited surfaces. *J. Opt. Soc. Am. B* **23**, 1954 (2006)
6. T. Pflug, M. Olbrich, A. Horn, Surface modifications of poly(methyl methacrylate) induced by controlled electronic and molecular vibrational excitation applying ultrafast mid-ir laser radiation. *J. Phys. Chem. C* **123**, 20210–20220 (2019)
7. J. Winter, D. Redka, J. Minár, M. Schmidt, H.P. Huber, Resolving transient temperature and density during ultrafast laser ablation of aluminum. *Appl. Phys. A* **129** (2023)
8. K.J. Schrider, B. Torralva, S.M. Yaliso, The dynamics of femtosecond pulsed laser removal of 20 nm Ni films from an interface. *Appl. Phys. Lett.* **107**, 124101 (2015)
9. T. Pflug et al., Laser-induced positional and chemical lattice reordering generating ferromagnetism. *Adv. Funct. Mater.* **34**, 2311951 (2023)
10. J. Hohlfeld et al., Electron and lattice dynamics following optical excitation of metals. *Chem. Phys.* **251**, 237–258 (2000)
11. T. Pflug et al., Fluence-dependent transient reflectance of stainless steel investigated by ultrafast imaging pump-probe reflectometry. *J. Phys. Chem. C* **125**, 17363–17371 (2021)
12. M. Olbrich et al., Hydrodynamic modeling and time-resolved imaging reflectometry of the ultrafast laser-induced ablation of a thin gold film. *Opt. Lasers Eng.* **129**, 106067 (2020)
13. S.-S. Wellershoff, J. Hohlfeld, J. Güdde, E. Matthias, The role of electron-phonon coupling in femtosecond laser damage of metals. *Appl. Phys. A* **69**, S99–S107 (1999)
14. N. Medvedev, I. Milov, Electron-phonon coupling in metals at high electronic temperatures. *Phys. Rev.* **B102** (2020)
15. J. Winter et al., Ultrafast pump-probe ellipsometry and microscopy reveal the surface dynamics of femtosecond laser ablation of aluminum and stainless steel. *Appl. Surf. Sci.* **511**, 145514 (2020)
16. M.E. Povarnitsyn, T.E. Itina, M. Sentis, K.V. Khishchenko, P.R. Levashov, Material decomposition mechanisms in femtosecond laser interactions with metals. *Phys. Rev. B* **75**, S95 (2007)
17. N.A. Inogamov et al., Two-temperature hydrodynamic expansion and coupling of strong elastic shock with supersonic melting front produced by ultrashort laser pulse. *J. Phys. Conf. Ser.* **500**, 192023 (2014)
18. F. Garrelie, F. Bourquard, A.-S. Loir, C. Donnet, J.-P. Colombier, Control of femtosecond pulsed laser ablation and deposition by temporal pulse shaping. *Opt. Laser Technol.* **78**, 42–51 (2016)
19. C.W. Cheng, S.Y. Wang, K.P. Chang, J.K. Chen, Femtosecond laser ablation of copper at high laser fluence: modeling and experimental comparison. *Appl. Surf. Sci.* **361**, 41–48 (2016)
20. L.J. Lewis, D. Perez, Laser ablation with short and ultrashort laser pulses: basic mechanisms from molecular-dynamics simulations. *Appl. Surf. Sci.* **255**, 5101–5106 (2009)

21. L.V. Zhigilei, Z. Lin, D.S. Ivanov, Atomistic modeling of short pulse laser ablation of metals: connections between melting, spallation, and phase explosion. *J. Phys. Chem. C* **113**, 11892–11906 (2009)
22. I. Milov et al., Two-level ablation and damage morphology of ru films under femtosecond extreme uv irradiation. *Appl. Surf. Sci.* **528**, 146952 (2020)
23. T. Pflug et al., Transient ablation topography of a thin chromium film after ultrashort pulsed laser irradiation in the spallation and phase explosion regime. *Opt. Laser Technol.* **172**, 110540 (2024)
24. J.P. Colombier, P. Combis, F. Bonneau, R. Le Harzic, E. Audouard, Hydrodynamic simulations of metal ablation by femtosecond laser irradiation. *Phys. Rev. B* **71**, 165406 (2005)
25. Y. Cao, Y.C. Shin, Multi-scale modeling of phase explosion in high fluence nanosecond laser ablation and clarification of ablation depth prediction criterion. *Appl. Surf. Sci.* **357**, 74–85 (2015)
26. C. Porneala, D.A. Willis, Effect of the dielectric transition on laser-induced phase explosion in metals. *Int. J. Heat Mass Transf.* **49**, 1928–1936 (2006)
27. T. Pflug, M. Olbrich, A. Horn, Electron dynamics in fused silica after strong field laser excitation detected by spectroscopic imaging pump-probe ellipsometry. *Phys. Rev. B* **106**, 014307 (2022)
28. J. Hernandez-Rueda, J. Siegel, M. Garcia-Lechuga, J. Solis, Femtosecond laser-induced refractive index changes at the surface of dielectrics: quantification based on newton ring analysis. *J. Opt. Soc. Am. B* **31**, 1676 (2014)
29. M.B. Agranat et al., Determination of the transport and optical properties of a nonideal solid-density plasma produced by femtosecond laser pulses. *J. Exp. Theor. Phys. Lett.* **85**, 271–276 (2007)
30. M.B. Agranat et al., Dynamics of plume and crater formation after action of femtosecond laser pulse. *Appl. Surf. Sci.* **253**, 6276–6282 (2007)
31. S.I. Ashitkov et al., Ablation and nanostructuring of metals by femtosecond laser pulses. *Quantum Electron.* **44**, 535–539 (2014)
32. N.A. Inogamov et al., Nanospallation induced by an ultrashort laser pulse. *J. Exp. Theor. Phys.* **107**, 1–19 (2008)
33. A.S. Zakharov et al., Interferometric diagnostics of ablation craters formed by femtosecond laser pulses. *J. Opt. Technol.* **69**, 478 (2002)
34. T. Pflug, Strong field excitation of electrons into localized states of fused silica: Techn. universität chemnitz. Dissertation (2021)
35. J.M. Liu, Simple technique for measurements of pulsed gaussian-beam spot sizes. *Opt. Lett.* **7**, 196–198 (1982)
36. M. Takeda, H. Ina, S. Kobayashi, Fourier-transform method of fringe-pattern analysis for computer-based topography and interferometry. *J. Opt. Soc. Am.* **72**, 156 (1982)
37. M. Olbrich, E. Punzel, P. Lickschat, S. Weißmantel, A. Horn, Investigation on the ablation of thin metal films with femtosecond to picosecond-pulsed laser radiation. *Phys. Procedia* **83**, 93–103 (2016)
38. N.A. Inogamov, V.V. Zhakhovsky, K.P. Migdal, Laser-induced spalling of thin metal film from silica substrate followed by inflation of microbump. *Appl. Phys. A Mater. Sci. Process.* **122**, 104910 (2016)

**Publisher's Note** Springer Nature remains neutral with regard to jurisdictional claims in published maps and institutional affiliations.